

We are IntechOpen, the world's leading publisher of Open Access books Built by scientists, for scientists

6,900

Open access books available

186,000

International authors and editors

200M

Downloads

Our authors are among the

154

Countries delivered to

TOP 1%

most cited scientists

12.2%

Contributors from top 500 universities



WEB OF SCIENCE™

Selection of our books indexed in the Book Citation Index
in Web of Science™ Core Collection (BKCI)

Interested in publishing with us?
Contact book.department@intechopen.com

Numbers displayed above are based on latest data collected.
For more information visit www.intechopen.com



Experimental Studies of Nanometer-Scaled Single-Asperity Contacts with Metal Surfaces

Arnaud Caron

Additional information is available at the end of the chapter

<http://dx.doi.org/10.5772/intechopen.72990>

Abstract

The contact between two surfaces initiates at surface asperities whose properties determine the mechanical behavior of the contact. The response of a nanometer-scaled single asperity onto flat surfaces is experimentally accessible using atomic force microscopy (AFM). The high spatial and force resolution of atomic force microscopy and spectroscopy enables to determine the mechanisms governing plastic deformation, friction, and wear down to the atomic scale. In this chapter, we describe three experimental methods based on atomic force microscopy and corresponding methods for statistical data analysis to determine: the hardness and the deformation mechanisms of metallic surfaces during indentation with an AFM tip and the mechanisms governing wear and friction of metallic surfaces.

Keywords: friction, wear, nanotribology, hardness, metals, atomic force microscopy

1. Introduction

Contact mechanical testing methods are the oldest techniques to characterize the mechanical response of materials [1]. The hardness of a material describes its resistance to the penetration of a harder indenter and correlates to its strength. Similarly, scratch hardness testing has long been used to describe the response of a material to the relative motion of a harder indenter sliding at the velocity v and under the action of a load F_n , thus enabling the study of friction and wear. According to Bowden and Tabor, friction and wear of metals are mediated either by the formation and shearing of junctions between surface asperities leading to their de-bonding or the plowing of a surface by a harder asperity leading to debris formation (see, e.g., Ref. [2]).

With the development of atomic force microscopy (AFM), the investigation of friction and wear between a smooth surface and a single asperity has become possible. This has allowed bridging the gap between macroscale experiments and the underlying tribological mechanisms that typically take place at the nm scale. At low load, single-asperity sliding friction of

metals has been observed to be governed by the dragging of nanoscale metallic junction giving rise to atomic stick-slip [3, 4]. The effects of surface-assembled monolayer (SAM) and oxidation on the nanotribology of Au(111) have been investigated and compared to the sliding friction behavior of an Au(111) surface [5]. It was shown that the formation of an Au neck at the Au (111)/tip interface determines the nanotribology of gold. Further, the authors have shown how the formation of such a neck can be suppressed by SAM and how the friction response of a gold surface can be switched by applying an electrochemical potential. In Refs. [6, 7], friction between Au islands and graphite was studied. $AF_n^{2/3}$ dependence of the friction force on gold islands measured in ambient conditions was observed, where F_n is the normal force [6]. These contrasts with results in Refs. [3, 4], where almost no frictional energy dissipation was measured. In this load regime also, the authors recently showed how the shear strength of such junctions can be tuned by changing the metallurgical affinity between the contact materials [7]. Also, nanoscale wear experiments by AFM demonstrated the determinant role of plastic deformation mechanisms [8, 9]. AFM indentation has proven to be a capable experimental method to resolve the atomistic mechanisms of plastic deformation [10–14]. For example, this method has been applied to study single dislocation activation in KBr(100) single crystals [10], Cu(100) [11], and Au(111) [12–14]. There, atomistic plasticity events were observed in the shape of pop-ins, with lengths in the range of 1 Å. More recently, AFM indentation has been combined with noncontact AFM to quantitatively determine the hardness and the fundamental mechanisms of plastic deformation of Au(111) [14], and Pt(111), and Pt-based metallic glass surfaces [15].

In this chapter, we describe three experimental methods based on atomic force microscopy and corresponding methods for statistical data analysis to determine the hardness and the mechanisms governing wear and friction of metallic surfaces.

2. Experimental setups and materials

The contact mechanical methods described in this chapter all rely on atomic force microscopy. The results presented below were obtained with two different instruments operated in different environments, i.e., ambient air and ultrahigh vacuum. Measurements in ambient air were performed using an XE-100 AFM manufactured by Park Systems, Republic of Korea. Measurements in ultrahigh vacuum were performed with a VT-AFM manufactured by Omicron Nano-Technology GmbH, Germany. **Figure 1** shows the respective schematics for each experimental setup. In both cases, a microfabricated cantilever with a sharp tip at its end is used to probe interaction forces with a sample surface. Depending on the physical properties of the tip and of the sample surface, various interaction forces can be probed: van der Waals, electrostatic, magnetic, and short-range forces [16]. In both experimental setups, such forces are measured using an optical beam deflection system. Thereby, a laser beam is reflected at the end of the cantilever onto a photodiode that yields an output voltage in proportion to the cantilever deflection. Typically, a four-segment photodiode is used. This enables to measure both normal and lateral forces according to.

$$F_n = C_n SV_{AB} \text{ and } F_l = \frac{3}{2} C_l \frac{h}{L} SV_{CD} \quad (1)$$

where S is the sensitivity of the photodiode, which we assume to be isotropic; V_{AB} and V_{CD} are the sum voltages for the photodiode segments indicated in the subscripts; C_n and C_l are, respectively, the bending and torsion stiffnesses of the cantilever; h is the tip height; and L is the cantilever length.

The setups illustrated in **Figure 1** mostly differ in the arrangement of their piezoelectric scanners. For the measurements in UHV, a sample tube xyz-scanner was used to both scan the sample surface and control the height of the cantilever or the interaction force between tip and sample. In the setup used for measurements in ambient conditions, a linear xy nanopositioning stage was used to scan the sample surface, while a separate linear z-scanner was used to control the height of the cantilever or the interaction forces between tip and sample.

In this work, the cantilever stiffnesses were determined either according to the geometrical beam theory [17] or following the thermal noise analysis [18]. According to the geometrical beam theory, $C_n = \frac{Ewt^3}{4L^3}$ and $C_l = \frac{Gwt^3}{3h^2L}$, where E is Young's modulus, G is the shear modulus, w is the width of the cantilever, and t its thickness. The length and the width of the cantilever can be measured by means of optical or electron microscopy. The thickness is usually determined from the first bending resonance frequency of the cantilever f_0 , with $t = \frac{2\sqrt{12}\pi}{1.875^2} \sqrt{\frac{\rho}{E} f_0 L^2}$, where ρ is the mass density. Alternatively, the normal stiffness can be determined from the mean square

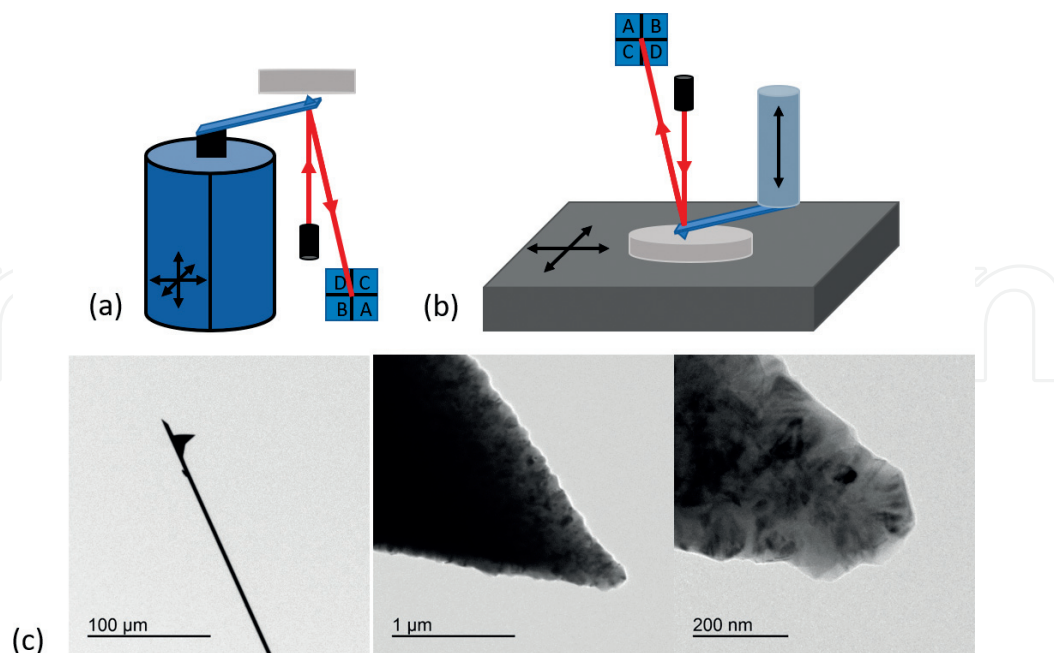


Figure 1. Experimental setups: instrumental setup used in (a) UHV and (b) ambient conditions; (c) TEM images of a typical diamond-coated Si single-crystalline AFM cantilever and its tip.

average of the thermal noise amplitude $\langle \overline{z^2} \rangle$ according to $C_n = \frac{k_B T}{\langle \overline{z^2} \rangle}$, where k_B is the Boltzmann constant and T the absolute temperature. The thermal noise vibrations of a cantilever beams can be recorded with the same optical beam deflection system as illustrated in **Figure 1**. The recorded signal consists in the superposition of all vibrational bending modes. It is important to note that the modes are not phase coherent. The identification of each mode is usually determined by fast Fourier transformation (FFT) of the time signal into a frequency spectrum (see **Figure 2**). In the case of the results shown in **Figure 2**, the power spectral density (PSD) function of the thermal noise amplitude was calculated by using the *psd* function of the MATLAB software. The area below the spectra then corresponds to the mean square of the thermal noise.

Experimental records of the thermal noise are, however, limited by the bandwidth of the photoelectric detector. In our experimental setups, the bandwidth of the detector is 2 MHz. The detection of the thermal noise is, however, further limited by the electrical noise level of the photoelectric detector. This becomes critical for higher frequent modes and stiffer structure in which case the vibration amplitude may be below the noise level of the detector. In this project, the electrical noise background of the photodetector was measured independently by reflecting the laser beam onto the photoelectric detector from a smooth surface of a bulk sample of the same material as used to manufacture the measured microstructures. As shown in **Figure 2(c)**, only the first two vibration modes of the cantilever can be identified. To account for the difficulty of analysis of higher vibration modes, the thermal noise analysis is usually restricted to the first mode. In this case, Eq. (1) can be multiplied by a weight factor:

$$\frac{3}{16} \alpha_1^2 \left(\frac{\sin \alpha_i + \sinh \alpha_i}{\sin \alpha_i \sinh \alpha_i} \right)^2 C_n \langle \overline{z_1^{*2}} \rangle = k_B T \quad (2)$$

where $\alpha_1 = 1.875$ is the dimensionless wavenumber of the first bending vibration mode (see Ref. [18] for more details).

To determine the stiffness of the cantilever, it is thus of utmost importance to accurately calculate the mean square amplitude of the thermal noise vibrations. The fast Fourier transformation (FFT) methods, such as implemented in the *psd* function, are usually applied to estimate the PSD function. Integrating the PSD function and using Eq. (2) to determine the cantilever stiffness from

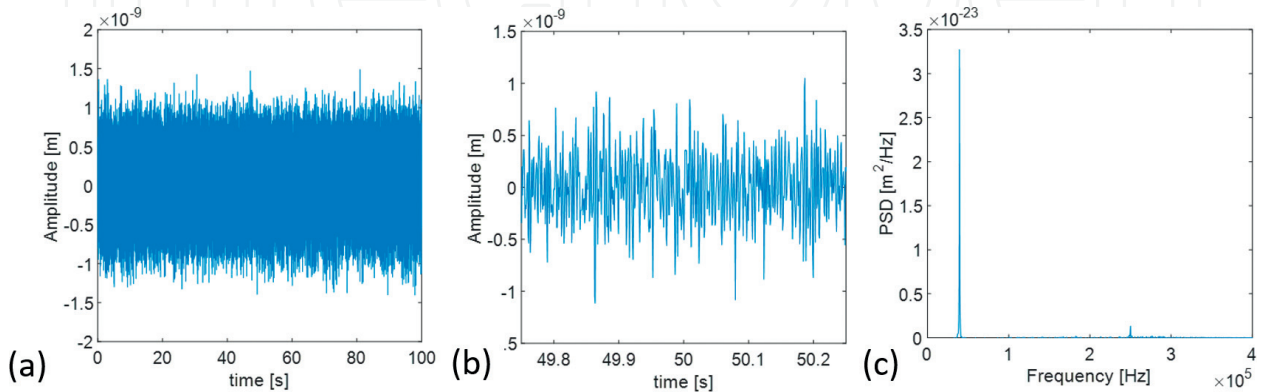


Figure 2. (a and b) Recorded time-dependent amplitude signals, (c) power spectral density (PSD) function of the signal shown in (a and b) and after background electrical noise removal.

the signals shown in **Figure 2** yield $\langle \overline{z_1^{*2}} \rangle = 4.32 \times 10^{-21} \text{ m}^2$ at $T = 293.15 \text{ K}$ and $C_n = 0.764 \text{ N/m}$. Similarly, the first peak of the PSD function can be fitted with the response function for a simple harmonic oscillator (SHO):

$$R(f) = \frac{A_1 f_1^4}{(f^2 - f_1^2)^2 + \left(\frac{f f_1}{Q_1}\right)^2} \quad (3)$$

where f_1 and Q_1 are the resonance frequency and the quality factor of the first peak and A_1 gives the zero-frequency amplitude of the SHO response [19]. Integration of the SHO response function over all frequencies provides an estimate of the cantilever stiffness if one only considers the lowest resonance mode:

$$\int_0^\infty R(f) df = \frac{\pi A_1 f_1 Q_1}{2} = \langle \overline{z_1^{*2}} \rangle = \frac{16k_B T}{3\alpha_1^2 C_n} \left(\frac{\sin \alpha_i \sinh \alpha_i}{\sin \alpha_i + \sinh \alpha_i} \right)^2 \quad (4)$$

Figure 3 shows the first peak of the PSD function and corresponds to fitting curve using Eq. (4) for the same measurement data plotted in **Figure 2**; we obtain $C_n = 0.814 \text{ N/m}$.

Atomic force microscopy imaging can either be performed in intermittent contact (tapping) or noncontact modes [20]. A detailed description of AFM operation in intermittent and noncontact modes is given elsewhere (see, e.g., Ref. [20]). In noncontact AFM an AFM cantilever is excited to its resonance frequency. The distance between tip and surface is kept in the range of a few

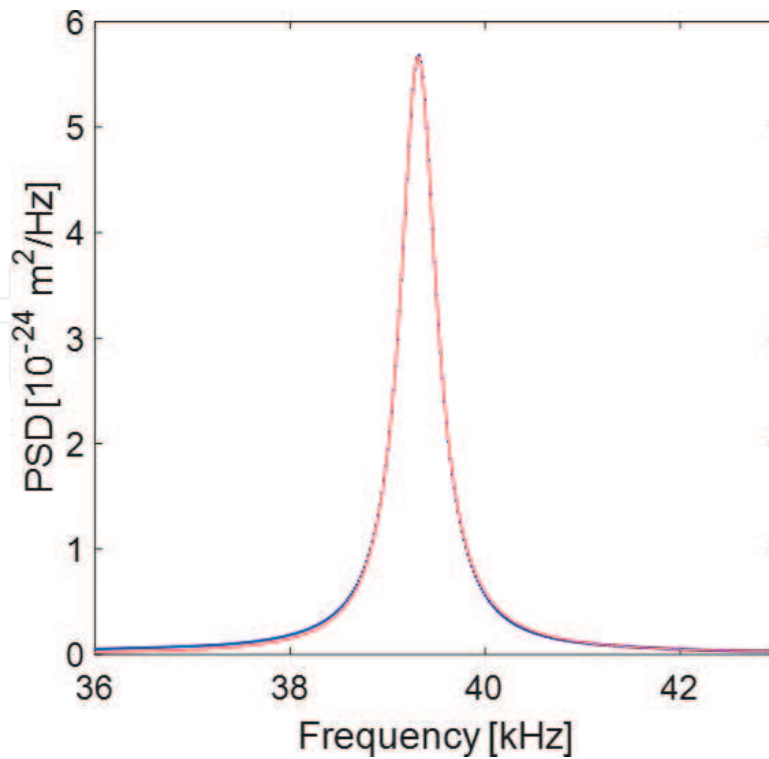


Figure 3. First peak of the PSD function shown in **Figure 2** and fitted with the response function for a simple harmonic oscillator.

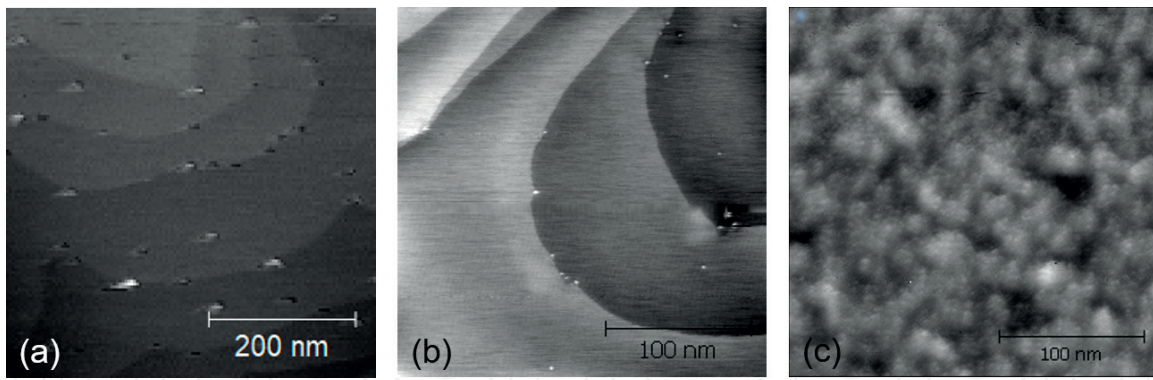


Figure 4. Topography images recorded by nc AFM on (a) Au(111), (b) Pt(111), and (c) $\text{Pt}_{57.5}\text{Cu}_{14.7}\text{Ni}_{5.3}\text{P}_{22.5}$ metallic glass surfaces.

nanometers. During scanning over a surface, changes in tip-sample distance due to sample topography result in changes in the amplitude and in a frequency shift of the cantilever resonance. To measure topography amplitude and/or frequency shift can be tracked by a feedback loop to keep the cantilever oscillation in resonance. Contact mode imaging relies on short-range interaction forces between the tip of a cantilever and the sample surface, the nature of which can be adhesive (attractive forces) or elastic (repulsive forces). During scanning, local changes in topography yield changes in the contact force between sample and surface. In this case, topography can be measured by tracking the normal contact force with a feedback loop to keep the contact force constant.

In this chapter, we present results obtained on single-crystalline metal and on metallic glass surfaces. An Au(111) polycrystalline thin film deposited on mica by physical vapor deposition was purchased by Phasis GmbH, Switzerland, and measured in ambient conditions (see Chapters III–V). Also, a Pt(111) surface and the surface of a $\text{Pt}_{57.5}\text{Cu}_{14.7}\text{Ni}_{5.3}\text{P}_{22.5}$ metallic glass were prepared for measurements in ultrahigh vacuum. The (111) surface of a platinum single crystal, purchased by MaTeck, Germany, was prepared by several cycles of Ar sputtering and annealing at 1000°C . This resulted in the formation of 50–100 nm wide atomically flat terraces. A $\text{Pt}_{57.5}\text{Cu}_{14.7}\text{Ni}_{5.3}\text{P}_{22.5}$ metallic glass master alloy was prepared according to [21] and subsequently melt-spun. The amorphousness of the as-prepared metallic glass ribbons was confirmed by X-ray diffraction (XRD) with Cu $K\alpha$ radiation and differential scanning calorimetry (DSC). To remove its native oxide layer, the surface of an as-prepared metallic glass ribbon was prepared by gentle Ar sputtering for 5 min with an energy of 1 keV.

All three sample surfaces were imaged by noncontact (nc) AFM to determine their respective RMS roughness R_q (see **Figure 4**). For atomically flat Au(111) and Pt(111), we found $R_q = 0.407$ nm and 0.372 nm, respectively, caused by atomic steps between terraces and adsorbates in the case of Au(111). For the Ar-sputtered $\text{Pt}_{57.5}\text{Cu}_{14.7}\text{Ni}_{5.3}\text{P}_{22.5}$ metallic glass, we found $R_q = 0.375$ nm.

3. AFM indentation for quantitative hardness measurements

The nanometer-scaled plastic deformation of Au(111), Pt(111), and $\text{Pt}_{57.5}\text{Cu}_{14.7}\text{Ni}_{5.3}\text{P}_{22.5}$ metallic glass was investigated by AFM indentation and subsequent nc AFM imaging. For indentation and

imaging, diamond-coated silicon single-crystalline cantilevers were used (type CDT-NCLR, manufactured by NanoSensors, Switzerland). For the cantilever used on Au(111), the bending stiffness was found to be $C_n = 55$ N/m. For AFM indentation of Pt(111) and Pt_{57.5}Cu_{14.7}Ni_{5.3}P_{22.5} metallic glass, a single cantilever of the same type as on Au(111) was used, whose normal stiffness was found to be $C_n = 46$ N/m.

Prior to the measurements on Au(111), the sensitivity S of the photodiode was calibrated by recording a force-distance curve on nanocrystalline diamond, consisting in an initial retraction of the z-scanner by 50 nm away from the sample surface and a subsequent series of approach and retraction by the same distance at a velocity of 0.3 $\mu\text{m/s}$. These parameters were set to avoid tip damages during contact between the diamond-coated tip and the nanocrystalline diamond sample. The sensitivity of the photodiode was then determined by fitting the repulsive part of the force-distance curve with a linear function. In contrast, before AFM indentation on Pt(111) and Pt_{57.5}Cu_{14.7}Ni_{5.3}P_{22.5} metallic glass, the sensitivity of the photodiode is calibrated in the noncontact mode of AFM, according to Ref. [22]. Thereby, we considered a conversion factor for the vibration energy of the cantilever determined from the optically measured deflection [17].

AFM indentation measurements consisted in recording the cantilever deflection upon extension of the z-scanner of the AFM. Owing to the tilt angle of the cantilever about the sample surface, a tilt correction was applied by moving the lateral scanner by $Z \times \tan \varphi$ during a vertical scanner extension Z , where $\varphi = 13^\circ$ is the tilt angle [23]. In this work the extension length Z of the z-scanner was varied from 10 to 160 nm in the case of Pt(111) and Pt_{57.5}Cu_{14.7}Ni_{5.3}P_{22.5} metallic glass and was set to $Z = 150$ nm for Au(111).

The plastic deformation of the three samples was analyzed based on nc AFM topographical images of the remaining indents and on the force-penetration curves. Typical topographical images of indented surfaces are shown for Au(111), Pt(111), and Pt_{57.5}Cu_{14.7}Ni_{5.3}P_{22.5} metallic glass in **Figure 5**. For each indent, the projected area was determined by masking the area with threshold height values. This analysis was performed with the indentation analysis function of the software package Gwyddion [24]. It is, however, important to note that due to convolution effects with the shape of the tip, the size of indents imaged by nc AFM is underestimated (this effect is more pronounced for smaller indents). Also, in the case of Pt_{57.5}Cu_{14.7}Ni_{5.3}P_{22.5} metallic glass, the prominence of the pileups makes an accurate determination of the projected area more difficult and less accurate.

The force-penetration ($F_n - \delta$) curves were calculated from the recorded force-distance ($F_n - Z$) curves (see **Figure 6**). The principle of AFM indentation relies on the fact that the surface to be indented is softer than the AFM tip. In this case, an extension of the z-scanner leads, besides a deflection D of the cantilever, to a penetration of the AFM tip into the sample surface by the penetration depth $\delta = Z - D$.

Figure 6 shows a series of nc AFM images of Au(111), Pt(111), and Pt_{57.5}Cu_{14.7}Ni_{5.3}P_{22.5} metallic glass surfaces after AFM indentation. In the case of Au(111), all indentations were performed with the same maximal load $F_n = 7$ μN and a same loading rate $dF_n/dt = 16$ $\mu\text{N/s}$. For Pt(111) and Pt_{57.5}Cu_{14.7}Ni_{5.3}P_{22.5} metallic glass surfaces, indentation is shown that was performed with varying maximum normal force values between $F_n = 0.8$ μN and $F_n = 6$ μN .

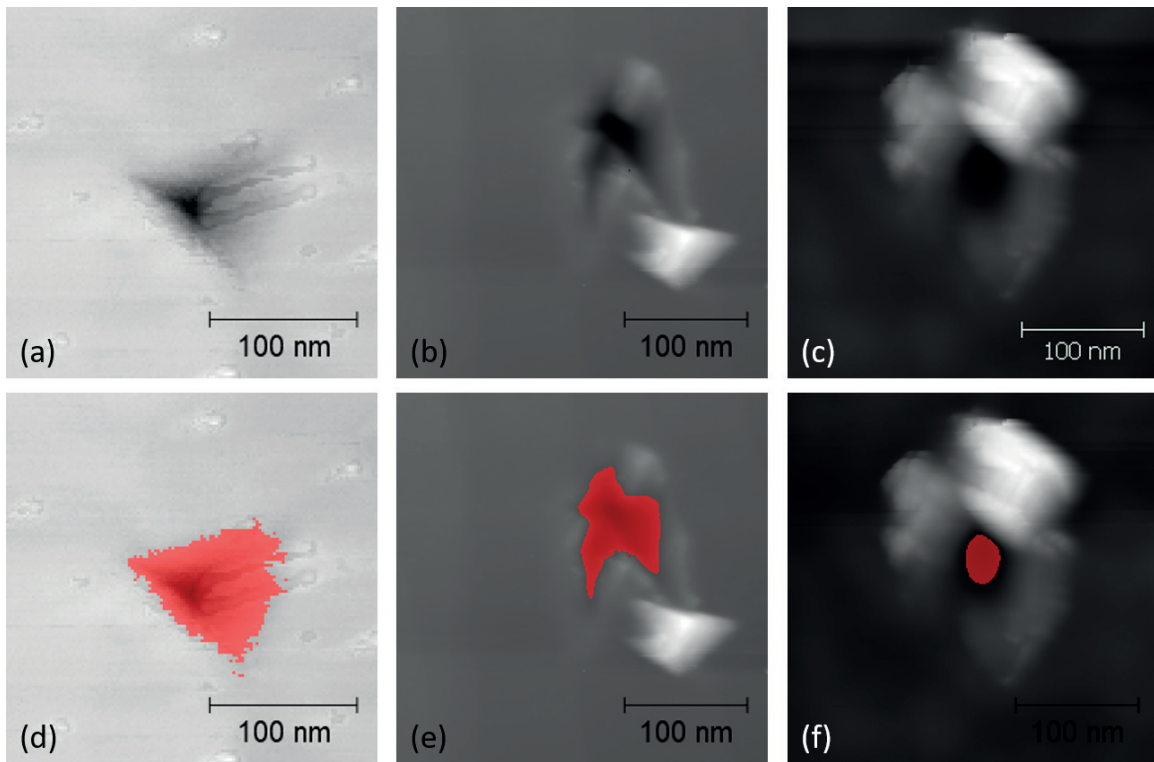


Figure 5. Nc AFM topography images of (a and d) Au(111), (b and e) Pt(111), and (c and f) $\text{Pt}_{57.5}\text{Cu}_{14.7}\text{Ni}_{5.3}\text{P}_{22.5}$ metallic glass surfaces after AFM indentation; in (d–f) the projected area was masked and calculated to determine the hardness values of each material.

For Au(111) two series of indentation measurements with the same maximum load values $F_n = 7.2 \mu\text{N}$ but with different tips are shown. Within both series, the shape and size of the remaining indents are very similar. For Pt(111) and $\text{Pt}_{57.5}\text{Cu}_{14.7}\text{Ni}_{5.3}\text{P}_{22.5}$ metallic glass, remaining indents were only observed for maximum load values $F_n > 0.8 \mu\text{N}$. For these two materials, the projected area of the indents is observed to increase with the maximal load.

In the case of Au(111), almost no pileup can be observed. In this case, clear dislocation can be identified around indents. In the case of Pt(111), small pileups can be observed. More importantly, above an indentation load $F_n = 3 \mu\text{N}$, the indent exhibits a chevron-like shape that was never observed on the two other samples and which attribute to anisotropic elastic relaxation of Pt(111). The pileups around indents on $\text{Pt}_{57.5}\text{Cu}_{14.7}\text{Ni}_{5.3}\text{P}_{22.5}$ metallic glass are much more prominent than on Au(111) or Pt(111). This indicates that the plastic deformation of Au(111) and Pt(111) was accommodated over much longer distances than in the case of the metallic glass. This view is also supported by the observation of dislocation lines on Au(111) that extends hundreds of nanometers away from the indents. In the case of the $\text{Pt}_{57.5}\text{Cu}_{14.7}\text{Ni}_{5.3}\text{P}_{22.5}$ metallic glass, plastic flow appears to be closely confined around the indenting tip.

Figure 7 shows indentation curves recorded on Au(111), Pt(111), and $\text{Pt}_{57.5}\text{Cu}_{14.7}\text{Ni}_{5.3}\text{P}_{22.5}$ metallic glass. In the case of Au(111) and Pt(111), the force-penetration curves overlap with each other, demonstrating the good reproducibility of the method. For those two materials, also the indentation curves show clear pop-ins that are attributed to the activation of dislocations. For $\text{Pt}_{57.5}\text{Cu}_{14.7}\text{Ni}_{5.3}\text{P}_{22.5}$ metallic glass, the force-penetration curves do not show any of pop-in. In this case, the deformation appears to be continuous.

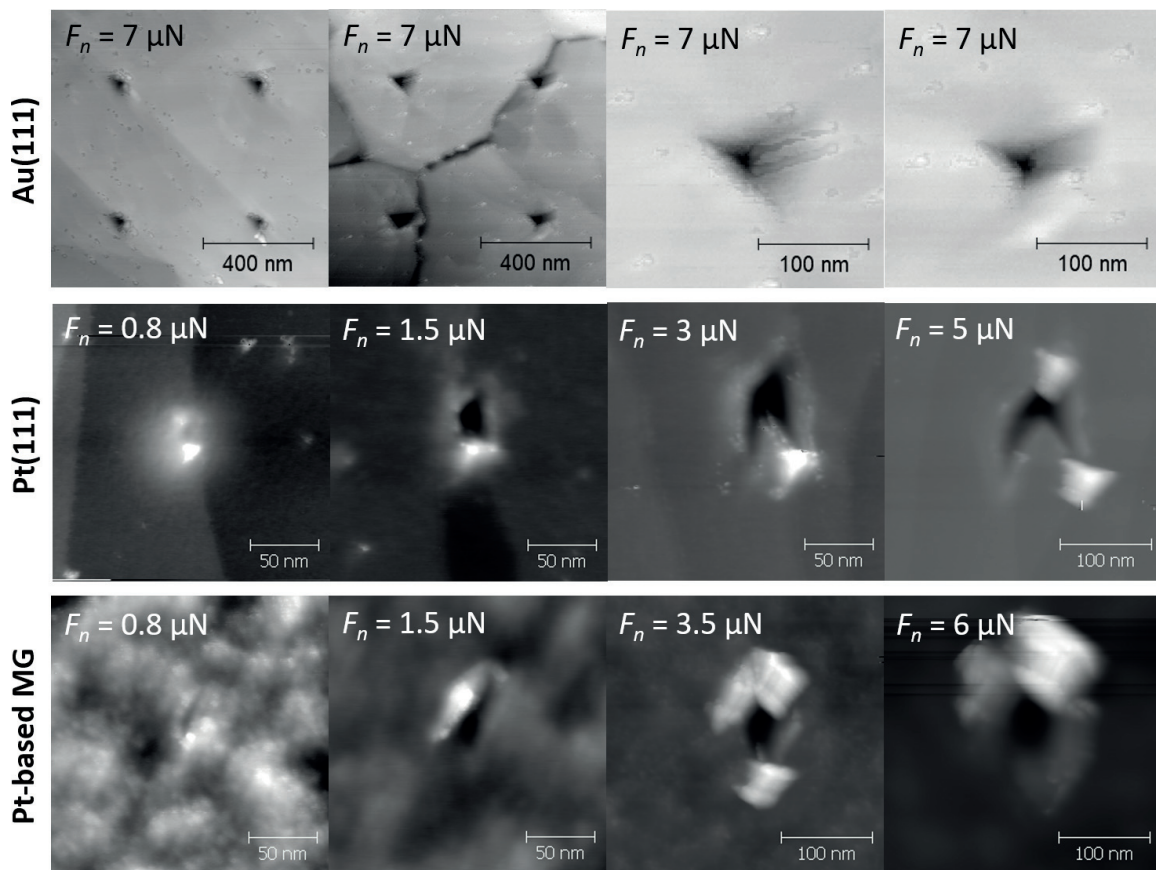


Figure 6. nc AFM topography images after AFM indentation measurements with the indicated normal force on Au(111), Pt(111), and Pt_{57.5}Cu_{14.7}Ni_{5.3}P_{22.5} metallic glass.

Figure 8 shows the load dependence of the projected area A_p for Pt(111) and Pt_{57.5}Cu_{14.7}Ni_{5.3}P_{22.5} metallic glass. The projected area A_p of indents is found to be much smaller for Pt_{57.5}Cu_{14.7}Ni_{5.3}P_{22.5} metallic glass than for Pt(111). Further, we used the load dependence of A_p to calculate the hardness of Pt(111) and Pt_{57.5}Cu_{14.7}Ni_{5.3}P_{22.5} metallic glass, according to $dA_p/dF_n = 1/H$. For Pt(111), we obtained $H = 1.14 \pm 0.09$ GPa. For Pt_{57.5}Cu_{14.7}Ni_{5.3}P_{22.5} metallic glass, we obtained $H = 7.3 \pm 2.4$ GPa. These values are larger than the measured ones by nanoindentation with a Berkovich diamond tip (see Ref. [15] for more details). This can be explained by tip convolution during nc AFM imaging that results in an underestimation of the projected area.

In the case of the indentation on Au(111), shown in **Figure 5**, we found $A_p = 4703.52$ nm², corresponding to $F_n = 7.2$ μN. Using the classical expression for the determination of hardness, we obtained $H = \frac{F_n}{A_p} = 1.53$ GPa. Alternatively, the shape of the AFM tip used to indent Au(111) was estimated from the noncontact AFM images shown in **Figure 6** with the free SPM data analysis software *Gwyddion* (**Figure 9**). The half-opening angle of the as-reconstructed indenter was determined to be $\alpha = 67.21^\circ$. The hardness was then calculated according to $H = \frac{F_n}{3\sqrt{3}\tan^2\alpha(\delta_{max}-\delta_{el})^2} = 1.46$ GPa [25], where δ_{max} is the maximal penetration depth in **Figure 7(a)**, and δ_{el} was taken as the penetration depth at the first pop-in event in **Figure 7(c)**. Both hardness calculations deliver virtually the same value: $H_{Au(111)} = 1.5$ GPa.

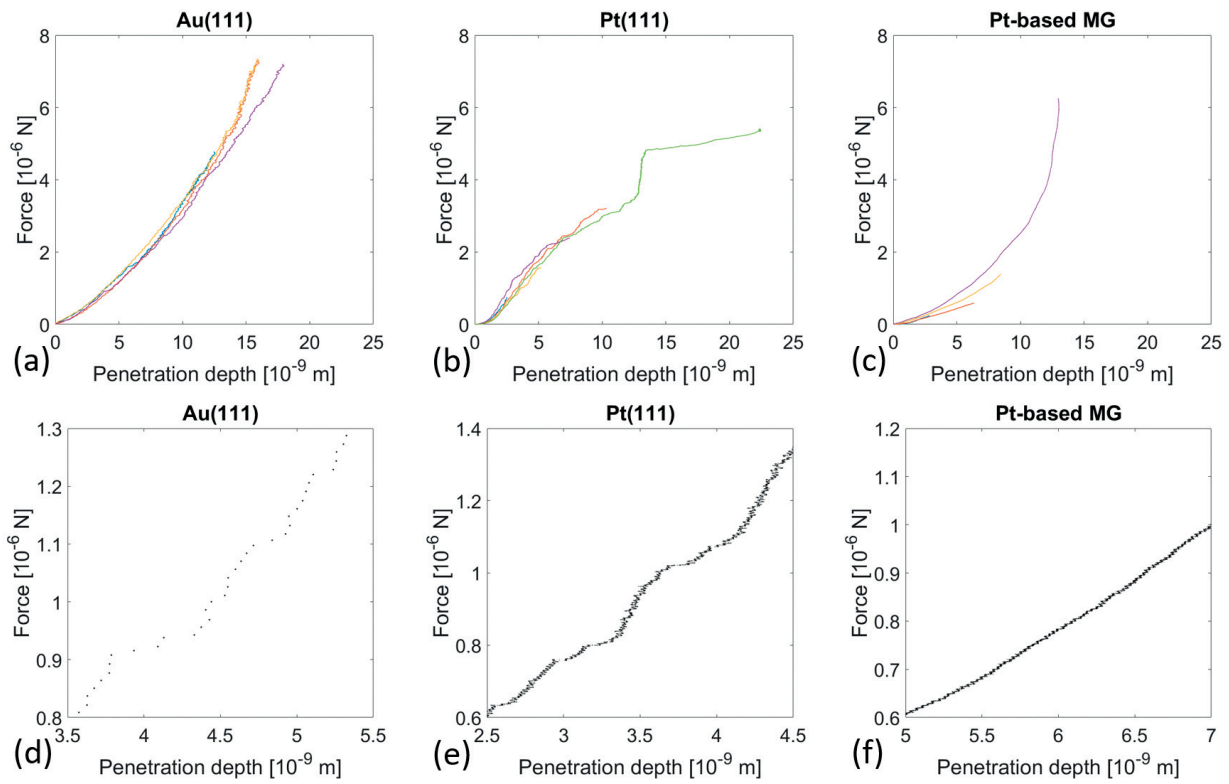


Figure 7. (a–c) Indentation curves and (d–e) magnification in the low load regime recorded on (a and d) Au(111), (b and e) Pt(111), and (c and f) $\text{Pt}_{57.5}\text{Cu}_{14.7}\text{Ni}_{5.3}\text{P}_{22.5}$ metallic glass.

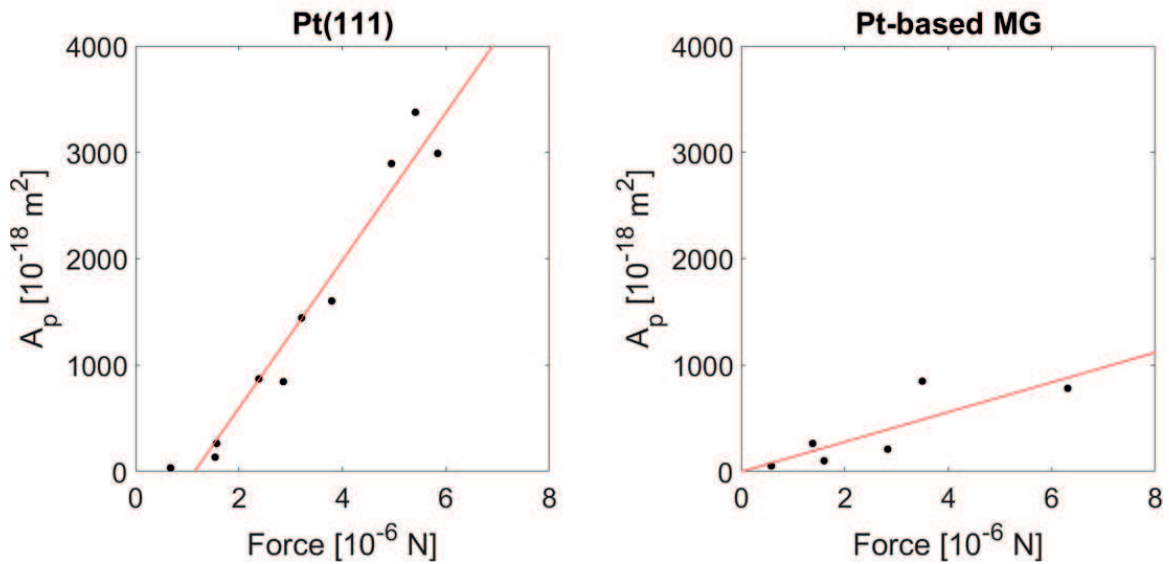


Figure 8. Indentation load dependence of the projected area A_p for (left) Pt(111) and (right) $\text{Pt}_{57.5}\text{Cu}_{14.7}\text{Ni}_{5.3}\text{P}_{22.5}$ metallic glass.

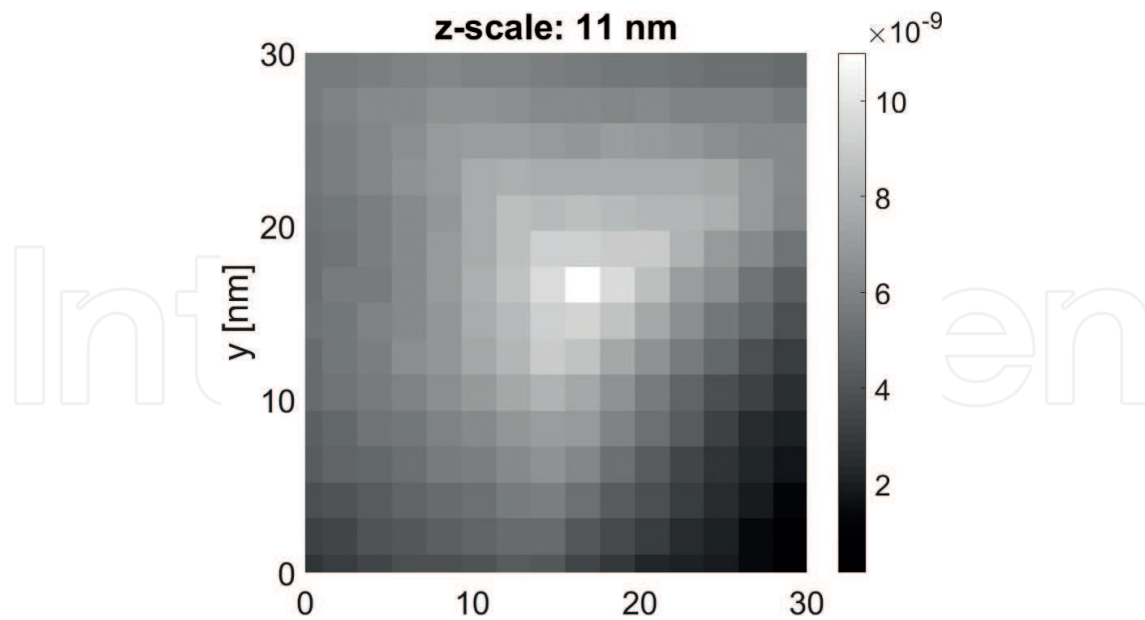


Figure 9. Estimated tip shape of the indenter used on Au(111).

4. AFM scratch test for friction and wear measurements

Wear and friction experiments were performed on Au(111) at room temperature and in ambient conditions ($T = 293$ K, $RH = 40\%$) by friction force microscopy (FFM) [26] with diamond-coated silicon cantilever (CDT-NCLR, manufactured by NanoSensors, Switzerland). The normal and lateral stiffnesses of the cantilevers, C_n and C_l , were determined from the geometrical beam theory; for the cantilever used on Au(111), we found $C_n = 50$ N/m and $C_l = 6954$ N/m. The sensitivity of the photodiode S was obtained by recording a force-distance curve on a non-compliant surface and fitting its repulsive part with a linear function. The normal and lateral forces were calculated from the vertical and lateral voltages of the photodiode, V_n and V_l , according to $F_n = C_n S V_n$ and $F_l = \frac{3}{2} C_l \frac{h}{L} S V_l$.

Wear and friction measurements consisted in reciprocal sliding over the same area $A_s = 2.5 \times 2.5$ μm^2 successively scanned over a load range $F_n = 20$ –4600 nN. The topography and the lateral force were recorded during the forward and backward cantilever motion along the fast-scan direction ($v = 10$ $\mu\text{m/s}$). Amplitude-modulated noncontact AFM topography images of the area subjected to tribological testing were recorded before and after measurements and compared to extract the wear volume by integration. Topographical changes during tribological testing were analyzed by correlating successively recorded topography images with the initial topography image recorded at the lowest load ($F_n = 20$ nN). Thereby, we used the *corrcoeff* function of the MATLAB software package to extract a correlation factor R . The slopes of the $R(F_n)$ -plot were further used to identify the transitions between wear mechanisms. Friction force images were calculated from the lateral force signals recorded in the forward and backward direction

according to $F_f = \frac{F_{l, fwd} - F_{l, bwd}}{2}$. In the case of Au(111), the probability distributions were calculated fitted with a Gaussian curve to provide the mean value and the standard deviation (see **Figure 10**). For the same ranges of normal force values as identified from the $R(F_n)$ -plots, coefficients of friction (COF) were determined from the linear slopes $COF = \frac{dF_f}{dF_n}$.

Figure 11 shows topography and friction force images simultaneously recorded on Au(111). Plastic deformation was observed to start at a load value $F_n = 129$ nN as indicated by the occurrence of dislocation lines in the corresponding topography image. Increasing the load to $F_n = 259$ nN resulted in an increased number of dislocation. In this load range, surface

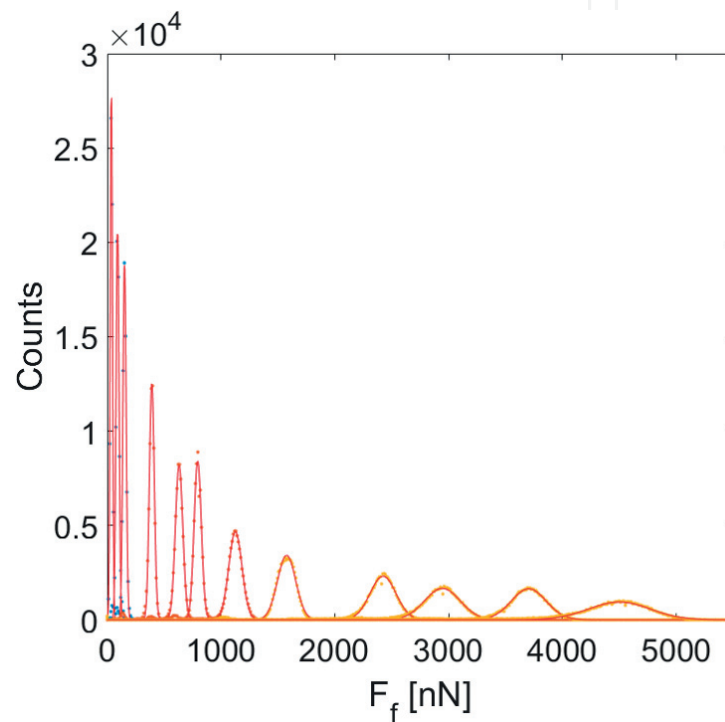


Figure 10. Probability distributions of friction force values measured at different normal force values. Each probability density distribution was fitted with a Gaussian function (red lines) to extract the mean friction force values and the corresponding standard deviation values.

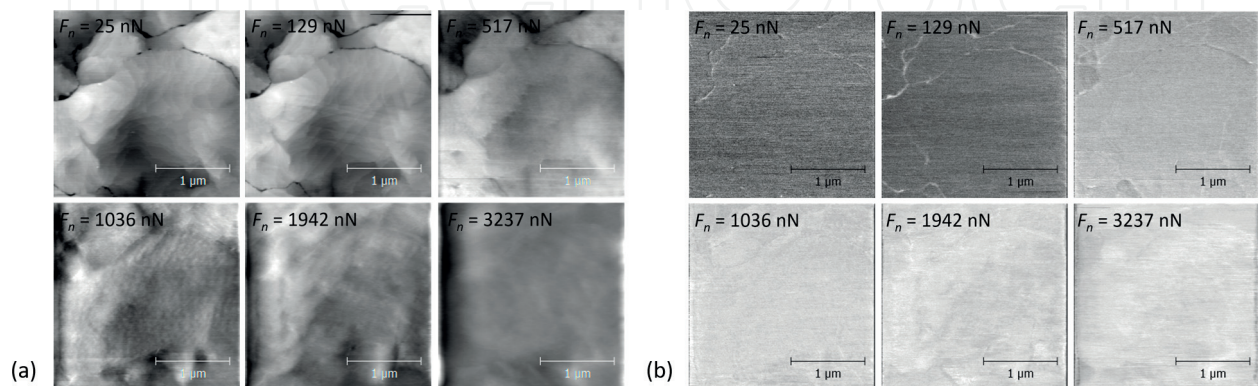


Figure 11. (a) Topography and (b) friction force images successively recorded on the same area of an Au(111) surface at the indicated loads.

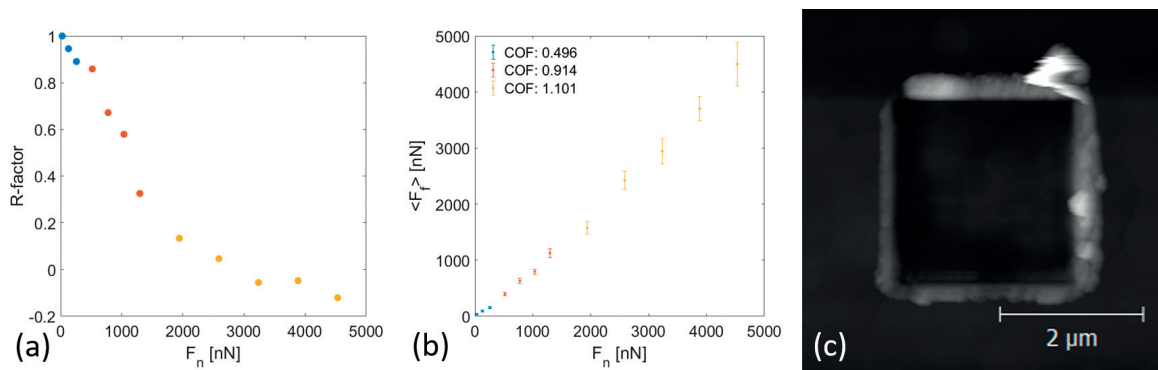


Figure 12. (a) Cross correlation factor R between the initial topography image in **Figure 11(a)** and the successive topography images recorded at the indicated load, (b) load dependence of friction, and (c) topography images of the area subjected to tribological tests (see **Figure 2(a)**).

topography features such as atomic steps remained clearly visible. This indicates in this load range that the sliding contact was rather governed by shearing and not plowing. In the load range $F_n = 517\text{--}1295$ nN, atomic steps were no longer observable, and a ripple structure was developed. In this load range, the mechanisms governing the sliding contact are considered to have a transition from shearing to plowing. In the range of the highest load values, $F_n = 1942\text{--}4531$ nN, pileups at the left and right side of the topography images became clearly observable. In this case, the governing mechanism was plowing. The three load ranges indicated above are illustrated in the $R(F_n)$ -plot, each of them being characterized by a different slope of decrease with increasing normal load $P = \frac{dR}{dF_n}$ (see **Figure 12(a)**).

Figure 11 also shows the friction force images corresponding to the topography measurements shown in the same figure. These images were further analyzed to determine the average friction force and its standard deviation (see above). **Figure 12(b)** shows the friction force F_f plotted against the normal force F_n . In the same figure, the error bars correspond to the standard deviation of the measurements. In agreement with the different load regimes determined in **Figure 12(a)**, the $F_f(F_n)$ -plot can be divided into different load ranges which corresponds a coefficient of friction $COF = \frac{dF_f}{dF_n}$. **Figure 12(c)** shows a noncontact AFM topography image of the area tested by contact AFM shown in **Figure 11**. The scratched surface exhibits pileups at the edges of the area scanned in contact. The corresponding wear volume was determined by integration of the height signal using the MATLAB software package. We calculated a wear volume $V_w = 0.0811 \mu\text{m}^3$ corresponding to an average wear depth of $\delta_w = 13$ nm.

5. Atomic-scale sliding friction measurements

Sliding friction experiments on Au(111) were performed in ambient conditions ($T = 293$ K, $RH = 40\%$) by FFM with a soft gold-coated AFM cantilevers of the type CONTSC-Au (manufactured by NanoSensors, Switzerland).

Prior to friction experiments, the sensitivity of the AFM photodiode S was determined following the same methods as above. The bending and torsion stiffnesses C_n and C_t of the cantilever were determined by thermal noise analysis. The cantilever stiffnesses are listed in **Table 1**.

Cantilever type	C_n [N/m]	C_t [N/m]	L^* [mm]	R^{**} [nm]
CONTSC-Au	0.685	136.24	225	25

*Manufacturer's data.

**Estimated data from SEM measurements.

Table 1. Cantilever properties.

The friction experiments consisted in recording the lateral deflection signal of the AFM cantilever in both forward and backward directions of the x -scanner. The experiments consisted in scanning an area of $10 \times 10 \text{ nm}^2$ with a normal load in the range $F_n = 0\text{--}10 \text{ nN}$ (**Figure 13**).

For each measurement, the friction force was calculated according to $F_f = \frac{F_{l, fwd} - F_{l, bwd}}{2}$, where $F_{l, fwd}$ and $F_{l, bwd}$ are the forward and backward images of the lateral force, respectively. Subsequently, the calculated friction force image was averaged line by line, and a corresponding error was calculated as the standard deviation from the mean value using the MATLAB software package. Moreover, the shear strength τ and the adhesion force F_{ad} were calculated by fitting the $F_f(F_n)$ -plot with the function $F_f = \tau A_c(F_n)$, where we consider τ to be constant and $A_c(F_n)$ is the normal force-dependent real area of contact between surface and tip (see Ref. [27]). Based on the Johnson-Kendall-Roberts (JKR) theory, the real area of an adhesive contact between a spherical elastic body and the flat surface of an elastic body can be expressed as $A_c = \pi \left(\frac{R}{E^*} \right)^{2/3} \left[(F_n - F_{ad}) + 2F_{ad} + \sqrt{4F_{ad}(F_n - F_{ad}) + (2F_{ad})^2} \right]^{2/3}$, where F_{ad} is the adhesion force between the two elastic bodies [28], R is the radius of the spherical body, $E^* = \left[\frac{1-\nu_1^2}{E_1} + \frac{1-\nu_2^2}{E_2} \right]^{-1}$ is the reduced modulus of elasticity, and E_i and ν_i are Young's moduli and Poisson's ratios of the two elastic bodies involved in the contact [29]. The resulting $F_n^{2/3}$ dependence of the friction force has been experimentally verified in Refs. [6, 27]. The following values were used for Young's modulus and Poisson's ratio: $E_{Au} = 75 \text{ GPa}$ and $\nu_{Au} = 0.44$.

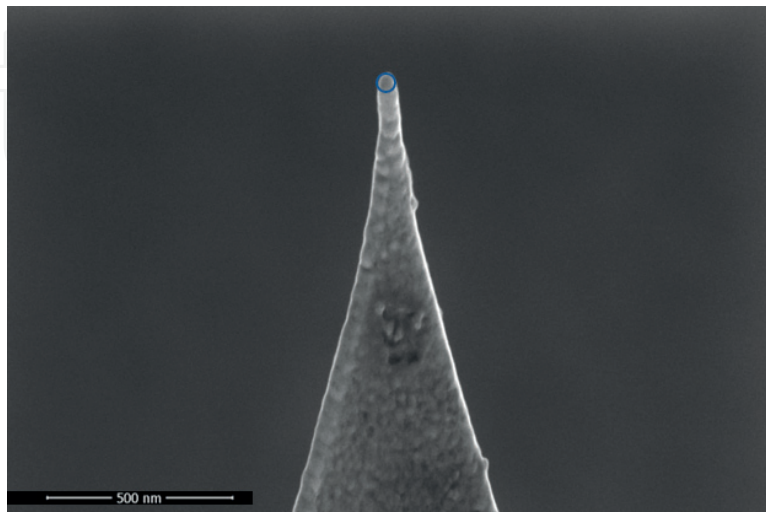


Figure 13. SEM image of the gold-coated AFM tip used friction measurements on Au(111).

In this work, the radius of curvature R of the AFM tip was determined by scanning electron microscopy (SEM) after the friction experiments (see **Figure 2** and **Table 1**) using a Helios 600i DualBeam FIB-SEM manufactured by FEI, Netherlands. A value $R \approx 25$ nm was found and used to fit the experimental $F_f(F_n)$ -plots. In **Figure 2**, a circle with a radius of 25 nm is overlaid to demonstrate the validity of this value.

Atomic-scale stick-slip was observed and statistically analyzed. The analysis consisted in line-by-line calculation of the power spectral density (PSD) function of each recorded $F_{l, fwd}$ images using the *psburg* function of the MATLAB software package. The calculated PSD functions corresponding to each line were averaged to provide a single PSD function out of one $F_{l, fwd}$ image. This statistical analysis transforms a signal in real space into a one-dimensional reciprocal space (k -space) signal, from which characteristic wavelengths $\lambda = 2\pi/k$ can be identified.

Figure 14 shows the load dependence of friction on Au(111) with an Au-coated tip. For this tribological couple, a shear strength value $\tau = 24.21$ MPa and an adhesion force value $F_{ad} = 25.8$ nN were calculated. Also, **Figure 3** shows a typical FFM image and corresponding forward and backward traces that exhibit periodic atomic scale stick-slip. In the following, the averaged power spectrum density (PSD) functions of the friction signals recorded at different loads were evaluated (see **Figure 15**). The PSD function corresponding to a typical friction measurement on Au(111) with an Au-coated tip shows a peak at a wavenumber $k = 21.36$ rad/nm. Neither the position nor the amplitude of this peak was found to change upon increasing load, except for $F_n = 10$ nN, in which case two slightly less prominent peaks were observed at $k = 20.11$ rad/nm and $k = 22.62$ rad/nm (see **Figure 15**).

Correspondingly, a characteristic wavelength $\lambda_2 = 0.294$ nm was calculated that well matches with the interatomic distance of Au in the [110] direction ($a_{[110]} = 288$ pm). The small discrepancy arises from the numerical approximation of the PSD function. The peak in the PSD functions was also found to split into two equidistant peaks at $F_n = 10$ nN, with corresponding wavelength values $\lambda_3 = 0.277$ nm and $\lambda_1 = 0.312$ nm, respectively. These peaks may correspond to the herringbone reconstruction of the Au(111) surface and the resulting different tilt angles of the fcc and hcp domains with respect to the unreconstructed surface [30].

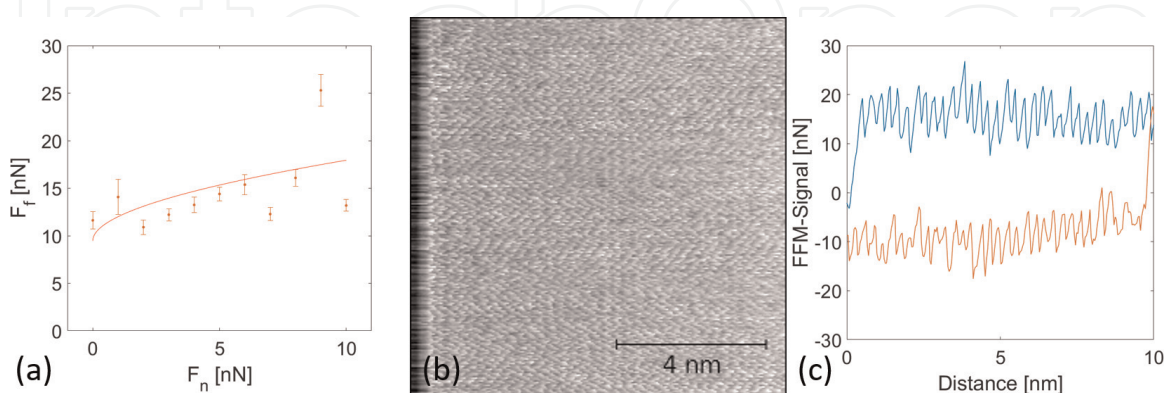


Figure 14. (a) Load dependence of friction and corresponding fit with a function of the type $F_f = \tau A_c(F_n)$, where τ is the shear strength and the real contact area A_c is expressed according to the JKR model [29]; (b) typical FFM image and (c) corresponding forward and backward traces exhibiting atomic scale stick-slip.

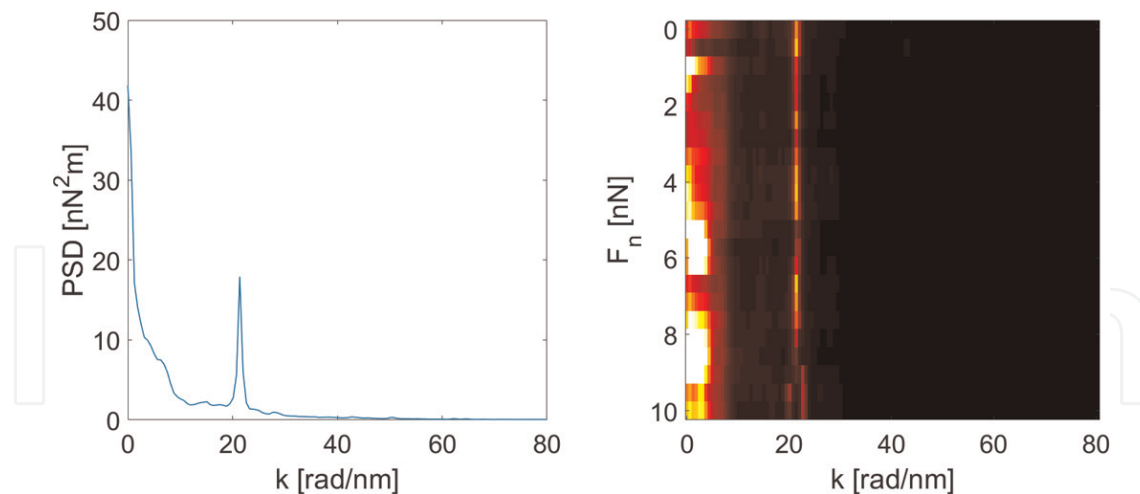


Figure 15. (Left) Typical power spectral density function calculated from FFM measurements on Au(111) with an Au-coated tip and (right) load dependence of the power density function as a function of the normal force F_n .

6. Conclusions

Experimental procedures based on atomic force microscopy to measure hardness, friction and wear, and the shear strength of metallic surfaces at the nanometer scale have been presented. AFM indentation was used to quantitatively and reproducibly determine the hardness and deformation mechanisms of Au(111), Pt(111), and a $\text{Pt}_{57.5}\text{Cu}_{14.7}\text{Ni}_{5.3}\text{P}_{22.5}$ metallic glass with unprecedented resolution in imaging and force curves. At the nanometer scale, the plastic deformation of single-crystalline metal surfaces is accommodated over large distances and mediated by dislocations. For $\text{Pt}_{57.5}\text{Cu}_{14.7}\text{Ni}_{5.3}\text{P}_{22.5}$ metallic glass, the nanometer-scaled plastic deformation is continuous and localized around the indenter; this contrasts with the observation of serrated flow at the μm scale.

AFM scratch testing was used to demonstrate the transitions between different wear regimes on Au(111) during single-asperity sliding contact. The coefficient of friction is found to increase with the severity of wear (from adhesive to abrasive). In the low load regime, wear is governed by adhesive effects, although in this regime the first dislocation lines could be observed. In the transitional regime, the formation of surface ripples was observed with the spacing between ripples increasing with the load. This regime corresponds to a transition from adhesive to abrasive wear, in which case materials start to be displaced ahead of the AFM tip. At larger loads, plowing is the governing mechanism. In this regime, the topography images are featureless, with exception of pileups at the side of the scanned area.

Atomic stick-slip images recorded on an Au(111) surface with a gold-coated tip were used to determine the shear strength of a metallic junction. By statistical analysis, we determined the periodicity of atomic stick-slip. Expectedly, it is found to correspond to the interatomic distance of gold.

Acknowledgements

The author is grateful to KOREATECH, Korea University of Technology and Education for the financial support. The author thanks Dr. M. Koch from Leibniz Institute for New Materials, Germany, for his help in providing TEM images of cantilevers.

Author details

Arnaud Caron

Address all correspondence to: arnaud.caron@koreatech.ac.kr

KoreaTech—Korea University of Technology and Education, Republic of Korea

References

- [1] Tabor D. *The Hardness of Metals*. Oxford, UK: Oxford University Press; 1951
- [2] Bowden FP, Tabor D. *The Friction and Lubrication of Solids*. Oxford, UK: Oxford University Press; 1950
- [3] Gosvami NN, Filleter T, Egberts P, Bennewitz R. Microscopic friction studies on metal surfaces. *Tribology Letters*. 2010;**39**:19-24
- [4] Gosvami NN, Feldmann M, Peguiron J, Moseler M, Schirmeisen A, Bennewitz R. Ageing of a microscopic sliding gold contact at low temperatures. *Physical Review Letters*. 2011; **107**:144303-1-144303-5
- [5] Bennewitz R, Hausen F, Gosvami NN. Nanotribology of clean and modified gold surfaces. *Journal of Materials Research*. 2013;**28**:1279-1288
- [6] Cihan E, Özogul A, Baykara MZ. Structure and nanotribology of thermally deposited gold nanoparticles on graphite. *Applied Surface Science*. 2015;**354**:429-436
- [7] Ko HE, Kwan SG, Park HW, Caron A. Chemical effects on the sliding friction of Ag and Au(111). *Friction*. 2017. <https://doi.org/10.1007/s40544-017-0167-5>
- [8] Caron A, Louzguine-Luzgin DV, Bennewitz R. Structure vs. chemistry: Friction and wear of Pt-based metallic surfaces. *ACS Applied Materials & Interfaces*. 2013;**5**:11341-11347
- [9] Ko HE, Park HW, Jiang JZ, Caron A. Nanoscopic wear behavior of face centered cubic metals. (Submitted to *Acta Materialia*)
- [10] Egberts P, Bennewitz R. Atomic scale nanoindentation: Detection and identification of single glide events in three dimensions by force microscopy. *Nanotechnology*. 2011; **22**(42):425703-1-425703-9
- [11] Filleter T, Bennewitz R. Nanometer scale plasticity of Cu(100). *Nanotechnology*. 2007;**18**(4): 044004-1-044004-4
- [12] Asenjo A, Jaafar M, Carrasco E, Rojo JM. Dislocation mechanisms in the first stage of plasticity of nanoindented Au(111) surfaces. *Physical Review B*. 2006;**73**(7):075431
- [13] Paul W, Oliver D, Miyahara Y, Gruetter P. Minimum threshold for incipient plasticity in the atomic-scale nanoindentation of Au(111). *Physical Review Letters*. 2013;**110**(13): 135506

- [14] Caron A. Quantitative hardness measurement by instrumented AFM-indentation. *Journal of Visualized Experiments*. 2016;**117**:e54706
- [15] Caron A, Bennewitz R. Lower nanometer-scale size limit for the deformation of a metallic glass by shear transformations revealed by quantitative AFM indentation. *Beilstein Journal of Nanotechnology*. 2015;**6**:1721-1732
- [16] Meyer E, Hug HJ, Bennewitz R. *Scanning Probe Microscopy: The Lab on a Tip*. Berlin, Heidelberg, Germany: Springer; 2004
- [17] Nonnenmacher M, Greschner J, Wolter O, Kassing R. *Journal of Vacuum Science and Technology B*. 1991;**9**:1358
- [18] Butt H-J, Jaschke M. Calculation of thermal noise in atomic force microscopy. *Nanotechnology*. 1995;**6**:1-7
- [19] Cook SM, Schaeffer TE, Chynoweth KM, Wigton M, Simmonds RW, Lang KM. Practical implementation of dynamics methods for measuring atomic force microscope cantilever spring constants. *Nanotechnology*. 2006;**17**:2135-2145
- [20] Voithlaender B. *Scanning Probe Microscopy: Atomic Force Microscopy and Scanning Tunneling Microscopy*. Berlin, Heidelberg, Germany: Springer; 2015
- [21] Schroers J, Johnson WL. Ductile bulk metallic glass. *Physical Review Letters*. 2004;**93**:255506
- [22] Giessibl FA. Direct method to calculate tip-sample forces from frequency shifts in frequency-modulation atomic force microscopy. *J. Applied Physics Letters*. 2001;**78**:123
- [23] Cannara RJ, Brukman MJ, Carpick RW. Cantilever tilt compensation for variable-load atomic force microscopy. *The Review of Scientific Instruments*. 2005;**76**:053706
- [24] <http://www.gwyddion.net>
- [25] Fischer-Cripps A, *Nanoindentation C*. 2nd ed. Springer: New York; 2004
- [26] Bennewitz R. Friction force microscopy. In: Gnecco E, Meyer E, editors. *Fundamentals of Friction and Wear*. Berlin, Heidelberg, Germany: Springer; 2007
- [27] Meyer E, Luethi R, Howald R, Bammerlin M, Guggisberg M, Guentherodt H-J. Site-specific friction force spectroscopy. *Journal of Vacuum Science and Technology B*. 1996;**14**:1285-1288
- [28] Johnson KL, Kendall K, Roberts AD. *Proceedings of the Royal Society of London. Series A*. 1971;**324**:301-313
- [29] Johnson KL. *Contact Mechanics*. Cambridge, UK: Cambridge University Press; 1985
- [30] Li Q, Dong Y, Martini A, Carpick RW. Atomic friction modulation on the reconstructed Au(111) surface. *Tribology Letters*. 2011;**43**:369-378